Doping by Design

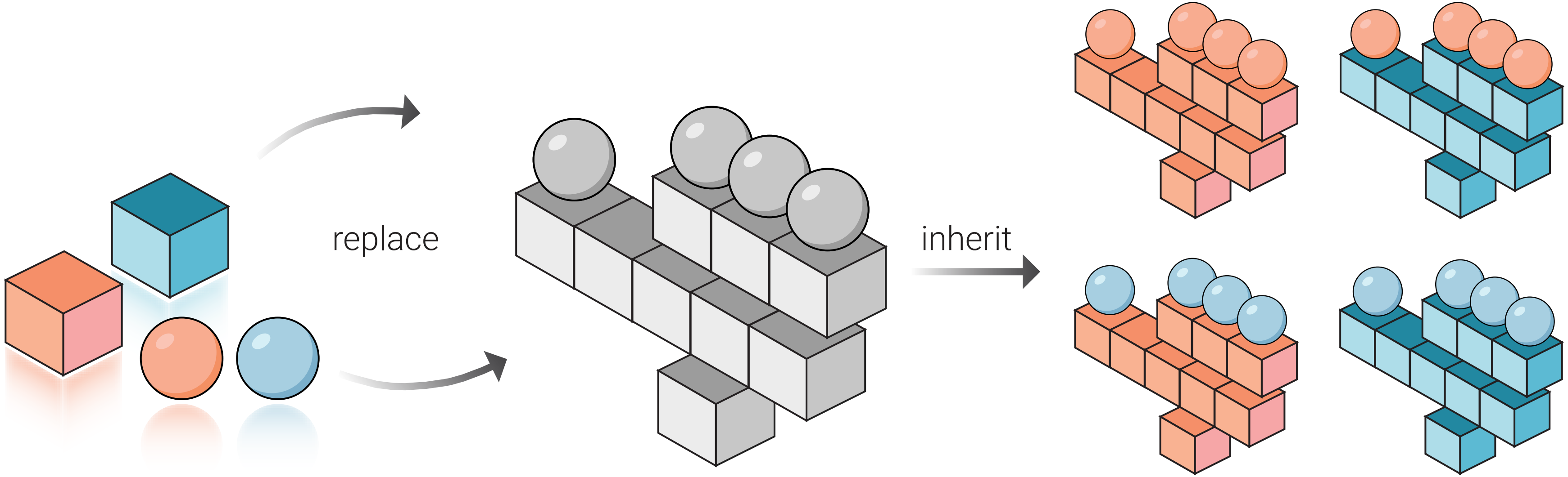

Plausible chemical substitutions

Prototype with desired doping characteristics

New materials with “designed” doping properties

Doping by Design: Finding New n-type Dopable ABX_4 Zintl Phases for Thermoelectrics

Jiaxing Qu,[a] Vladan Stevanović,[b] Elif Ertekin,[a] Prashun Gorai[b*]

Doping remains a bottleneck in discovering novel functional materials for applications such as thermoelectrics (TE) and photovoltaics. The current computational approach to materials discovery is to identify candidates by predicting the functional properties of a pool of known materials, and hope that the candidates can be appropriately doped. What if we could "design" new materials that have the desired functionalities and doping properties? In this work, we use an approach, wherein we perform chemical replacements in a prototype structure, to realize doping by design. We hypothesize that the doping characteristics and functional performance of the prototype structure are translated to the new compounds created by chemical replacements. Discovery of new n-type Zintl phases is desirable for TE; however, n-type Zintl phases are a rarity. We demonstrate our doping design strategy by discovering 7 new, previously-unreported ABX_4 Zintl phases that adopt the prototypical $KGaSb_4$ structure. Among the new phases, we computationally confirm that $NaAlSb_4$, $NaGaSb_4$ and $CsInSb_4$ are n-type dopable and potentially exhibit high n-type TE performance, even exceeding that of $KGaSb_4$. Our structure prototyping approach offers a promising route to discover new materials with designed doping and functional properties.

1 Introduction

Doping has been an enduring and pervasive challenge in the discovery of new functional materials for thermoelectrics,[1,2] transparent conductors,[3,4] photovoltaics,[5,6] etc. There are several challenges in doping materials: (1) cannot be sufficiently doped with either electrons (n-type) or holes (p-type) i.e., material is an insulator, or (2) cannot be doped with the desired carrier type (doping asymmetry), or (3) cannot be doped to the desired carrier concentration needed for the specific application. For instance, wide band gap oxides such as SiO_2 and Al_2O_3 are insulators that cannot be doped either n- or p-type. Some materials suffer from doping asymmetry, wurtzite ZnO being one of the prominent examples. While n-type doping of ZnO is achieved by Al doping, p-type doping remains elusive.[7] Doping asymmetry has practical implications. ZnSb is predicted to be a promising n-type TE material;[8] however, it has been shown theoretically[9] and experimentally[10] that n-type doping cannot be achieved. The low formation energy of acceptor Zn vacancies lead to degenerate p-type doping behavior of ZnSb.[9]

Within intermetallic compounds, there exists a subset known as Zintl phases that generally exhibit doping asymmetry. To date, most well-known Zintl phases with moderate carrier concentrations are native p-type due to self-doping. However, only a few n-type ones have been reported in experiments.[11–14] The inherent features of Zintl phases, such as small band gaps, dispersive electronic bands, and complex structures, make them suitable as TE materials. Zintl phases such as $Yb_{14}MnSb_{11}$,[15] $CaZn_2Sb_2$[16] and $Ca_5Al_2Sb_6$[17] are among the TE materials with best performance in mid- to high-temperature regime. The experimental data in Figure 1 demonstrates the well-known doping asymmetry in Zintl phases. The maximum electronegativity difference is a measure of the bonding ionicity between the cation-anion framework. The p-type Zintl phases, denoted by blue markers, outnumber the n-type phases (red markers).

Computational predictions indicate that Zintl phases when doped n-type have comparable or better TE performance than their p-type versions.[11] However, the discovery of new n-type Zintl phases so far has been driven by chemical intuition and serendipity. The recent discoveries of new n-type Zintl phases, including $KAlSb_4$,[11] $KGaSb_4$,[12] $RbGaSb_4$,[13] $CsGaSb_4$,[13] and $Ba_3Cd_2P_4$,[14] seem to suggest that (1) there are Zintl phases that may overcome the doping asymmetry, and (2) the chemical and structural phase space of n-type Zintl phases is largely underexplored. One plausible route for finding new n-type dopable Zintl phases with high TE performance is by chemical replacements in structure prototype (CRISP).[19] Computational efforts in the past have utilized chemical substitution in known compounds to search for undiscovered phases.[20,21] In the last decade, various routes have been explored to search for as-yet-unknown materials for functional applications.[22–25] These studies served the general purpose of discovering new compounds rather than new compounds with designed functionalities.

In this work, we show that chemical substitutions in appropriately chosen prototype structures is a viable route to discover new compounds with designed doping properties. Selecting an appropriate prototype structure is one of the key aspects of this approach. The prototype should possess the same functionality (e.g. high TE performance) and doping (e.g. n-type dopable) characteristics that we desire to "transfer" to the new compounds

---

[a] *University of Illinois at Urbana-Champaign, Urbana, IL 61801.* [b] *Colorado School of Mines, Golden, CO 80401.* [*] *E-mail: pgorai@mines.edu*

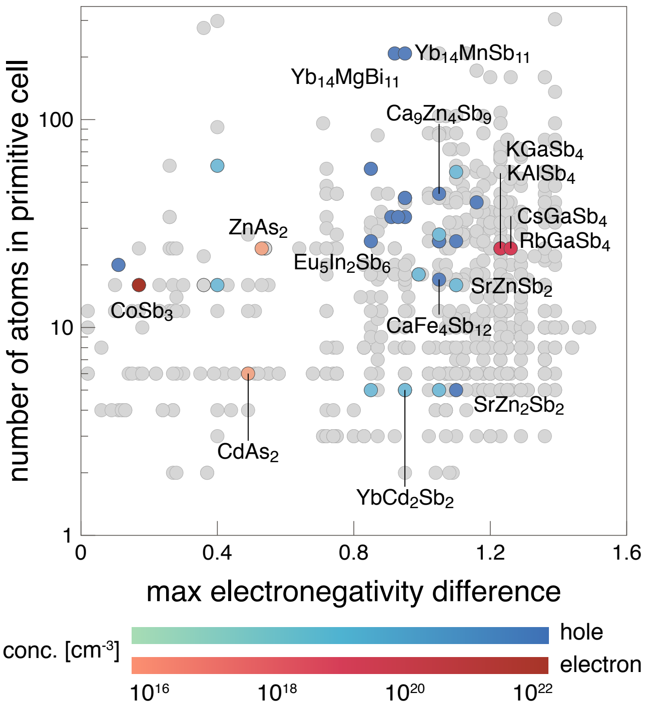

Fig. 1 Binary and ternary Zintl phases from the ICSD represented by the number of atoms in the primitive cell and the maximum electronegativity difference (on the Pauling scale) between the constituent elements. The color scheme denotes the experimentally measured charge carrier concentrations of 46 Zintl phases, with blue denoting p-type (hole) and red n-type (electron). KGaSb$_4$ and CoSb$_3$ can be doped both n- and p-type; only n-type is shown for clarity. n-type Ba$_3$Cd$_2$P$_4$ is not shown because carrier concentration has not been measured yet.[14] Data adapted from Ref. [18], with permission from the Royal Society of Chemistry.

created by chemical substitutions. We demonstrate this approach to discover new ABX$_4$ Zintl phases (A = Na, K, Rb, Cs; B = Al, Ga, In; X = As, Sb, Bi) that adopt the KGaSb$_4$ prototype structure (Figure 2), predicted to have high TE performance and are n-type dopable. KGaSb$_4$ serves as an appropriate prototype for two reasons: (1) it has good n-type TE performance, with $zT \sim 1$, and (2) can be doped n-type to $>10^{19}$ cm^{-3} electron concentrations.[12] Out of the 36 plausible Zintl phases, only 2 are reported in the Inorganic Crystal Structure Database (ICSD)[26] and four of them have been recently discovered,[13] indicating that the phase space of KGaSb$_4$ type Zintl phases is under-explored. Importantly, the 6 known ABX$_4$ phases are all n-type dopable.[12,13] Using first-principles calculations, we theoretically evaluate the thermodynamic and dynamic stability of the 36 ABX$_4$ Zintl phases and predict that 13 of them should be stable, including the 6 known phases (KGaSb$_4$, KAlSb$_4$, CsGaSb$_4$, CsAlSb$_4$, RbGaSb$_4$, RbAlSb$_4$) and 7 new phases. Of the 7 undiscovered phases, we choose the top 3 candidates (NaAlSb$_4$, NaGaSb$_4$ and CsInSb$_4$) that are predicted to have the highest n-type TE performance; first-principles defect calculations reveal that they are all n-type dopable.

2 Methods

The computational workflow is summarized in Figure 3. We create hypothetical Zintl phases by chemical replacements in the prototype KGaSb$_4$ structure and relax them with DFT. Next, we calculate their electronic structures and theoretical TE performance. Subsequently, we assess the thermodynamic and dynamic stability of those structures with predicted high n-type TE performance. Finally, we assess the n-type dopability of the top candidates using first-principles defect calculations.

2.1 Chemical Replacements in Prototype Structure

Chemical substitutions are performed in the prototype structure KGaSb$_4$ to create hypothetical ABX$_4$ compounds. With consideration to nominal oxidation states and electronegativity, we choose alkali elements Na, K, Cs, and Rb for the **A** site, group 13 elements (Al, Ga, In) for the **B** site, and pnictides (As, Sb, Bi) for the X site. The orthorhombic crystal structure of KGaSb$_4$ (*Pnma*) consists of an anionic framework formed by GaSb$_4$ tetrahedra linked by Sb-Sb covalent bonds. K atoms occupy the channels formed by the anionic framework (Figure 2). The small electronegativity difference between Ga and Sb ($\Delta\chi_{\mathrm{Ga-Sb}}$ = 0.24 on Pauling scale) gives rise to the covalent nature of the anionic frameworks, while the high electropositivity of K ($\Delta\chi_{\mathrm{K-Sb}}$ = 1.23) leads to ionic bonding with the anionic frameworks i.e., electron transfer from K to the anionic framework.

2.2 Structure Relaxation and Electronic Structure

The hypothetical structures generated using chemical substitutions are relaxed with density functional theory (DFT) using the plane-wave VASP code.[27] The Perdew-Burke-Ernzerhof (PBE) exchange correlation functional[28] is used within the generalized gradient approximation (GGA). The core and valence electrons are treated with the projector-augmented wave (PAW) method.[29] The hypothetical structures are relaxed with a plane-wave en-

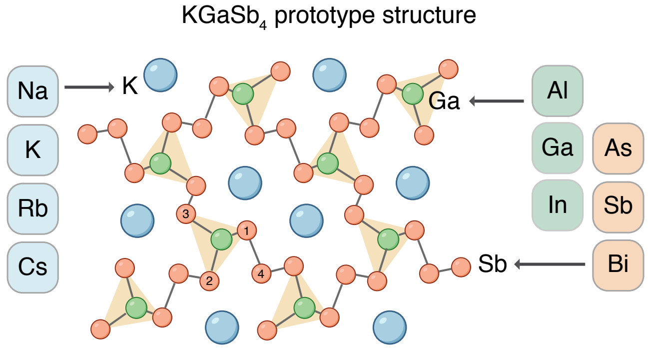

Fig. 2 Crystal structure of KGaSb$_4$, a Zintl phase with an anionic framework composed of [GaSb$_4$] tetrahedra linked by homoatomic Sb–Sb bonds. K atoms occupy the channels formed by the anionic framework. We perform chemical replacements in the prototypical KGaSb$_4$ structure, where K is replaced with Na, K, Rb, Cs, Ga with Al, Ga, In, and Sb with As, Sb, Bi. Sb has four unique Wyckoff sites, labelled 1 through 4.

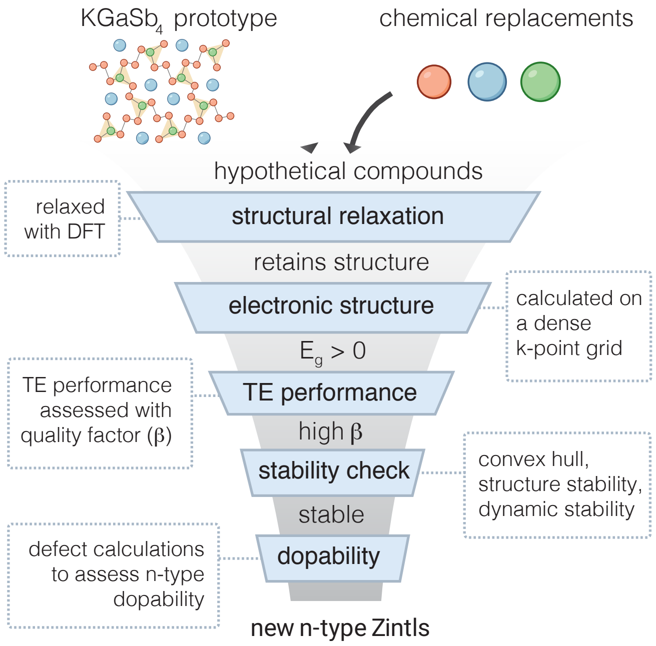

Fig. 3 Schematic computational workflow of chemical replacements in structure prototype approach. Here, E_g is the band gap and β is the predicted thermoelectric quality factor, a measure of thermoelectric performance. Specifically, the n-type β is considered.

ergy cutoff of 340 eV and a Monkhorst-Pack k-point sampling. The space groups of the relaxed structures are then determined to check whether they retain the prototype structure. Electronic structures are calculated on a dense k-mesh with a fixed number of k-points. The k-point grid is determined according to the equation: $N_{\mathrm{atoms}} \times N_{\mathrm{kpts}} \simeq 8000$, where N_{atoms} is the number of atoms in the primitive cell and N_{kpts} is the number of k points. Structures with zero DFT-calculated band gaps are not considered in the subsequent steps. Therefore, hypothetical compounds that retain the prototype structure and have non-zero band gaps are considered for further analysis.

2.3 Thermoelectric Performance Assessment

The quality factor (β) provides a measure of the potential for thermoelectric performance of a material. We have previously developed semi-empirical models to computationally evaluate β (see Ref. 30 for details). The quality factor is expressed in terms of the electronic and lattice thermal transport parameters as:

$$\beta \propto \frac{\mu_0 {m^*_{\mathrm{DOS}}}^{3/2}}{\kappa_L} T^{5/2} \tag{1}$$

where μ_0 is the intrinsic charge carrier mobility at 300 K, m^*_{DOS} the density-of-states (DOS) effective mass, and κ_L the lattice thermal conductivity at 300 K. Semi-empirical models of μ_0 and κ_L allow computational assessment of the quality factor[30,31] with first-principles calculations. To determine μ_0 and κ_L from the semi-empirical models, band degeneracy (N_b), DOS effective mass (m^*_{DOS}) and bulk modulus (B) need to be determined. The parabolic band approximation is used to extract m^*_{DOS} within a 100 meV energy window away from the band edge positions. With m^*_{DOS} and N_b, the band effective mass (m^*_b) can be determined within the parabolic and isotropic band approximation: $m^*_b = m^*_{\mathrm{DOS}} N_b^{-2/3}$. Bulk modulus B is obtained by fitting the Birch-Murnaghan equation of state.[32] κ_L is calculated using a semi-empirical model based on the modified Debye-Callaway model;[31] the model inputs are bulk modulus (B), density, volume per atom, average atomic mass, average coordination number, and the number of atoms in the primitive cell. Besides B, the other model parameters are directly accessible from the structure.

2.4 Stability Assessment

Compositional Stability: Stability against chemical decomposition into competing phases can be assessed with convex hull analysis. The energies of ABX$_4$ compositions as well as different binary and ternary competing phases are calculated. Materials on the convex hull are stable. The energy above the convex hull (ΔE_{hull}) is an indicator of the compositional stability of the ABX$_4$ phase. If the ABX$_4$ phase lies on the hull or within 20 meV/atom from the hull, it is deemed to be compositionally stable. The competing phases are searched within the ICSD.[26] The total energies of the competing phases are calculated by relaxing the structures with the same methodology as described in Section 2.2. The formation enthalpies are calculated from the total energies and reference chemical potentials of the elemental phases. The reference chemical potentials are obtained by fitting to a set of experimentally measured formation enthalpies, similar to the procedure described in Ref. 33, which has been shown to provide accurate predictions for formation enthalpies. See supplementary material for the fitted reference chemical potentials.

Structural Stability: The aim of the structural stability analysis is to find if the lowest-energy (most favorable) structure for a given ABX$_4$ composition is the prototype structure. Plausible structures are selected from the ICSD[26] that can accommodate 1-1-4 ternary stoichiometries. In order to identify plausible 1-1-4 stoichiometry structures, we impose further the following constraints: cations on A and B sites with compatible oxidation states (1+ for A, 3+ for B). To assess structural stability, each ABX$_4$ composition is fully relaxed in all plausible structures chosen from ICSD, including in the prototype KGaSb$_4$ structure. Structure relaxation is performed as described in Section 2.2. The most favorable structure is the lowest-energy structure; if the prototype KGaSb$_4$ structure is the lowest-energy structure, then the ABX$_4$ composition is deemed structurally stable.

Dynamic Stability: For ABX$_4$ Zintl phases that are found to be compositionally and structurally stable, we test their dynamic stability w.r.t. Γ-point phonons using density functional perturbation theory (DFPT), as implemented in VASP.[27] The structures are relaxed with a plane-wave energy cutoff of 520 eV with an energy convergence criterion of 10^{-8} eV. The Brillouin zone is sampled using a Γ-centered 4×4×2 Monkhorst-Pack k-point grid. Structures with no imaginary frequencies at Γ point are considered dynamically stable. We also calculate the full phonon dispersion for

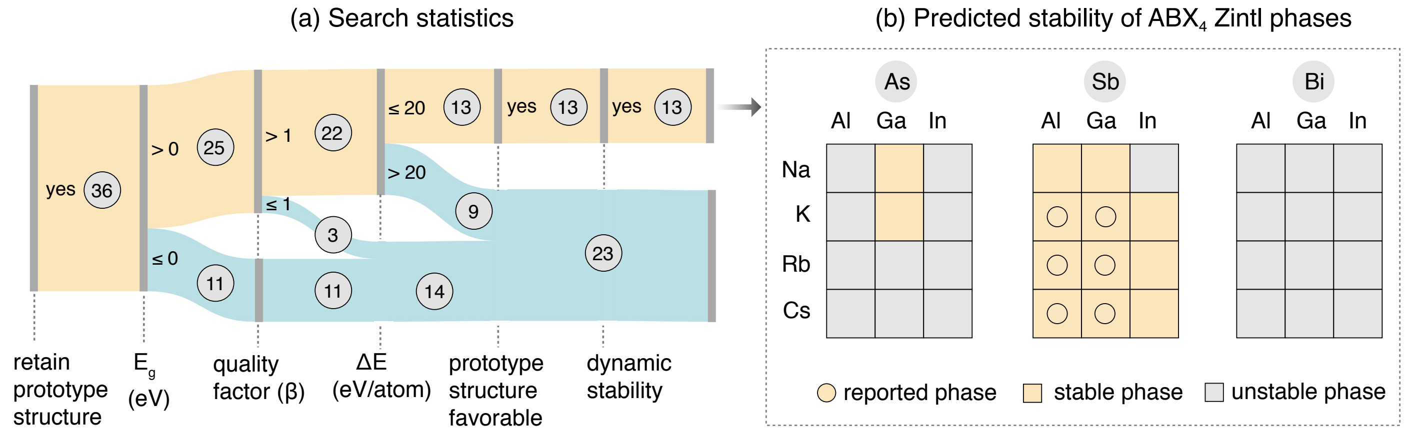

Fig. 4 Statistics of the search for new ABX$_4$ Zintl phases: (a) Sankey plot of the material screening, resulting in the identification of 13 stable phases, including the 6 known and 7 newly predicted phases. (b) Chemical search space of 36 ABX$_4$ Zintl phases, with known phases (from ICSD or reported in Ref. 13) denoted by circles. Yellow and grey boxes correspond to stable and unstable phases from our stability predictions, respectively.

three stable ABX$_4$ phases using the supercell finite-displacement method implemented in the Phonopy package,[34,35] with VASP as the force calculator. The self-consistent calculations in VASP are performed with the same plane-wave energy cutoff and k-point grid as the DFPT calculation, with an energy convergence criterion of of 10^{-8} eV.

2.5 Defect energetics

To understand the defect chemistry of ABX$_4$ Zintl phases, we employ the standard supercell approach[36] to calculate the defect formation energies of native point defects. The defect formation energy ($\Delta H_{D,q}$) is calculated from the total energies as follows:

$$\Delta H_{\mathrm{D},q} = E_{\mathrm{D},q} - E_{\mathrm{host}} + \sum_i n_i \mu_i + qE_{\mathrm{F}} + E_{\mathrm{corr}} \qquad (2)$$

where $\Delta H_{\mathrm{D},q}$ represents the formation energy of a defect D in charge state q; $E_{\mathrm{D},q}$ and E_{host} are the total energies of the supercell with and without the defects, respectively, E_{F} is the Fermi energy which varies from the valence band maximum (VBM) to the conduction band minimum (CBM), E_{corr} is the term that accounts for the finite-size corrections within the supercell approach, μ_i is the chemical potential of elemental species i added ($n_i < 0$) or removed ($n_i > 0$) from the host supercell to form defects. The elemental chemical potential μ_i is expressed as $\mu_i = \mu_i^0 + \Delta\mu_i$, where μ_i^0 is the reference elemental potential (see Section 2.4) and $\Delta\mu_i$ the deviation from the reference elemental phase. The bounds on $\Delta\mu_i$ are set by the thermodynamic stability condition, with $\Delta\mu_i = 0$ corresponding to i-rich conditions and a large negative value of $\Delta\mu_i$ represents i-poor growth conditions.

First-principles defect calculations are performed using the GGA-PBE exchange correlation functional. The Brillouin zone of the 192-atom supercells is sampled using a Γ-centered $2 \times 2 \times 2$ k-grid. The atomic positions in the defect supercells are fully relaxed to obtain the total energies. The following corrections to the defect formation energies are included in E_{corr} as described in Ref. 36: (1) image charge correction for charged defects, (2) potential alignment correction for charged defects, (3) band-filling corrections for shallow defects, and (4) band gap correction. The static dielectric constant (electronic + ionic), which is needed for calculating the image chare correction, is evaluated using DFPT. To correct the band gap under-estimation in GGA-PBE, we employ state-of-art GW quasiparticle energy calculations to compute the band edge shifts relative to the DFT band edge positions.[37] A computational framework for automation of point defect calculations, pylada-defects,[38] is utilized in this work for creating the defect supercells and analysis of the results, including calculation of finite-size corrections.

The formation energies for the native point defects (vacancy, anti-site defect, interstitial) are calculated in charge states q = -3, -2, -1, 0 , +1, +2, and +3. All unique Wyckoff positions in the crystal structures (Figure 2) are considered in the calculations for vacancies and anti-site defects. The likely interstitial sites are determined by a Voronoi tessellation scheme, as implemented in pylada-defects.[38] In each structure, we consider up to 20-25 possible interstitial sites and then determine the lowest-energy site based on total energies of the relaxed supercells. The free carrier concentrations at specific temperatures are calculated self-consistently by solving the charge-neutrality conditions.

3 Results and Discussion

Figure 4(a) presents the summary of the computational search of new ABX$_4$ Zintl phases in the prototypical KGaSb$_4$ structure. Out of the 36 phases considered in this study, only 6 are known/reported,[11–13] indicating that the chemical phase space of ABX$_4$ compound is under-explored. From electronic structure calculations, we find that 25 out of 36 ABX$_4$ phases (in the assumed KGaSb$_4$ structure) have non-zero DFT band gap (Figure 4a). Furthermore, 22 out of 25 have n-type β larger than that of PbTe, a well-known thermoelectric material. Of the remaining 22 compositions, we find that 13 of them are stable - compositionally (within 20 meV/atom from the convex hull), structurally (most favorable in KGaSb$_4$ structure), and dynamically (no imag-

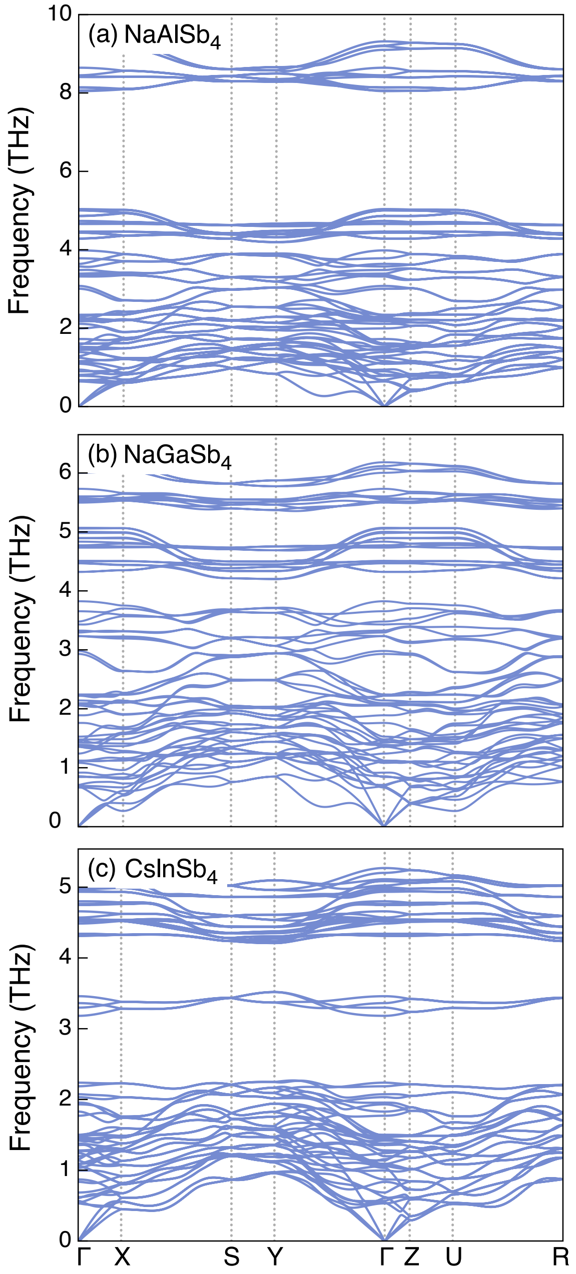

Fig. 5 Phonon dispersions of (a) $NaAlSb_4$, (b) $NaGaSb_4$ and (c) $CsInSb_4$ along the special k-point paths of the Brillouin zone of an orthorhombic lattice.

inary phonon frequencies).

3.1 Stability Assessment

Our stability analysis reveals 13 stable ABX_4 phases that are either on or within 20 meV/atom from the convex hull (Table 1), most stable in the $KGaSb_4$ prototype structure, and dynamically stable w.r.t. Γ-point phonon modes. These 13 phases include the 6 known/reported phases ($KAlSb_4$,[11] $KGaSb_4$,[12] $CsAlSb_4$,[13] $CsGaSb_4$,[13] $RbAlSb_4$,[13] and $RbGaSb_4$,[13]) and 7 as-yet-unknown phases ($NaAlSb_4$, $NaGaAs_4$, $KGaAs_4$, $NaGaSb_4$, $KInSb_4$, $RbInSb_4$, $CsInSb_4$). Through our stability assessment, we correctly predict the existence of the 6 known experimentally synthesized phases, which lends credence to our stability predictions. Among the 13 stable phases, 8 of them lie on the hull while the remaining 5 are above the hull but within 20 meV/atom (Table 1). These predicted stable compounds comprise of 2 arsenides and 11 antimonides. We find that all the bismuthides are thermodynamically unstable, which is consistent with synthesis attempts in Ref. 13. Our convex hull analysis shows that the primary competing phases, which restrict the compositional stability of the ABX_4 phases, are ternary $A_2B_2X_3$ phases. For instance, $Na_2Al_2Sb_3$ and NaSb competes with $NaAlSb_4$ under Na-rich growth condition.

For establishing structural stability, we consider 34 plausible structures from the ICSD[26] using the criteria explained in the Methods (Section 2.4). The full list of the 34 structures are provided in the Supplementary Information. We perform the structural stability analysis on all 13 compositionally stable phases and find that all of them are structurally stable in the prototype $KGaSb_4$ structure. Furthermore, we find that all 13 phases are dynamically stable at Γ-point (see Supplementary Information).

To further confirm the dynamic stability, we calculated the full-path phonon dispersions of the 3 newly predicted phases - $NaAlSb_4$, $NaGaSb_4$ and $CsInSb_4$ (see in Figure 5). See Section 3.3 for the reasons why we choose these three candidate materials. The absence of imaginary phonon modes in the phonon bandstructure further confirms the dynamic stability of $NaAlSb_4$, $NaGaSb_4$ and $CsInSb_4$. As expected, the low-energy modes are dominated by contributions from the heavy element Sb. The phonon dispersions (Figure 5) feature low-energy optical modes (<1 THz) that appear to hybridize with the acoustic modes. It has been shown that such acoustic-optical hybridization can lead to increased scattering of the primary heat-carrier acoustic modes, resulting in low lattice thermal conductivities.[39]

3.2 Electronic Structure of ABX_4 Phases

Figure 6 presents the electronic band structures of $NaAlSb_4$, $NaGaSb_4$, and $CsInSb_4$. The band structures are plotted along the special k-point paths of the orthorhombic Brillouin zone. The band gap underestimation in DFT is adjusted by applying band edge shifts calculated with GW quasi-particle energy calculations (see Section 2.5). $NaAlSb_4$, $NaGaSb_4$, and $CsInSb_4$ are all small band gap semiconductors (<1 eV), which is typical of Zintl phases. $CsInSb_4$ has a larger band gap compared to $NaAlSb_4$ and $NaGaSb_4$ owing to the larger electronegativity difference between Cs and In. In all three phases, there exist conduction band (CB) valleys at Γ and at Z. In $NaAlSb_4$ and $NaGaSb_4$, there are additional CB valleys along Γ-Y ($N_b = 2$) and Γ-Z ($N_b = 2$) that also lie within the 100 meV energy window from the CBM shown by the red shaded region in Figure 6. In $NaAlSb_4$ and $NaGaSb_4$, the CBM lie along Γ-Z while in $CsInSb_4$, the CBM is located at Γ. The electronic structure of other ABX_4 phases is available in Supplementary Information.

When band valleys (or pockets) do not lie at special k-points, it increases band degeneracy due to symmetry. Consequently, $NaAlSb_4$ and $NaGaSb_4$ have high conduction band degeneracies of 6 and 7, respectively. High band degeneracy coupled with low band effective mass enhances charge transport properties for

Phases	$\beta/\beta_{\mathrm{PbTe}}$ (n-type)	$N_{\mathrm{b,CB}}$	κ_{L} (W/mK)	μ_{n} (cm^2/Vs)	ΔE_{hull} (meV/atom)
$NaGaSb_4$	4.8	7	1.0	88	7
$NaAlSb_4$	4.5	6	1.0	124	17
$CsInSb_4$	1.7	2	1.2	136	0
$CsGaSb_4^*$	1.7	2	0.9	117	0
$RbInSb_4$	1.6	2	1.2	141	0
$KInSb_4$	1.6	2	1.3	150	4
$CsAlSb_4^*$	1.5	2	0.9	98	0
$RbGaSb_4^*$	1.5	2	0.9	105	0
$KGaSb_4^*$	1.5	2	1.0	106	0
$RbAlSb_4^*$	1.4	2	1.0	88	0
$KGaAs_4$	1.4	2	1.4	123	12
$KAlSb_4^*$	1.3	2	1.0	93	0
$NaGaAs_4$	1.2	2	1.4	93	19

Table 1 Computed electronic structure parameters, transport properties, and thermoelectric performance of 13 ABX_4 Zintl phases that are predicted to be stable in the $KGaSb_4$ structure. β (n-type) is referenced to n-type β of PbTe (15), $N_{\mathrm{b,CB}}$ is conduction band degeneracy, κ_{L} is room-temperature lattice thermal conductivity, μ_n is room-temperature electron mobility (in cm^2/Vs) and ΔE_{hull} is the energy above the convex hull. * denotes the known ABX_4 phases.

thermoelectrics, including high carrier mobility (low band effective mass) and high thermopower (high DOS effective mass).

3.3 Predicted Thermoelectric Performance

Figure 7 presents the predicted n-type thermoelectric performance of the 13 stable ABX_4 phases; the 7 newly predicted ABX_4 phases are labeled. The computed intrinsic electron mobility (μ_e) is plotted as a function of the lattice thermal conductivity (κ_{L}), with the color scheme representing the CB degeneracy ($N_{\mathrm{b,CB}}$) in Figure 7(a) and the DOS effective mass ($m^*_{\mathrm{DOS,CB}}$) in Figure 7(b). The size of the markers scales with n-type β. The β for n-type PbTe is shown for reference in Figure 7(a). In general, we find that the 13 ABX_4 phases exhibit low κ_{L} (<1.5 W/mK) and high μ_e (75 to 150 cm^2/Vs), which indicates that ABX_4 Zintl phases are promising n-type materials for thermoelectrics.

The predicted transport properties and TE performance assessment are summarized in Table 1, sorted in the descending order of their n-type β values. All 13 compounds in Table 1 have relatively high n-type TE performance - larger β than PbTe, when optimally doped. $NaGaSb_4$ and $NaAlSb_4$ stand out as the most promising candidates with the highest normalized $\beta/\beta_{\mathrm{PbTe}}$ of 4.8 and 4.5, respectively. The high predicted n-type TE performance of $NaGaSb_4$ and $NaAlSb_4$ can be primarily attributed to their high conduction band degeneracy of 7 and 6, respectively, which is larger than that of other ABX_4 phases ($N_{\mathrm{b,CB}} = 2$). Coupled with moderately low CB effective mass (0.072 for $NaAlSb_4$ and 0.090 for $NaGaSb_4$), the high band degeneracy leads to high DOS effective mass, as shown in Figure 7(b). The full assessment of transport properties and TE performance of the 13 ABX_4 phases is available in the Supplementary Information. The data will be also made available on our thermoelectrics-focused open-access database, TEDesignLab (www.tedesignlab.org).[40]

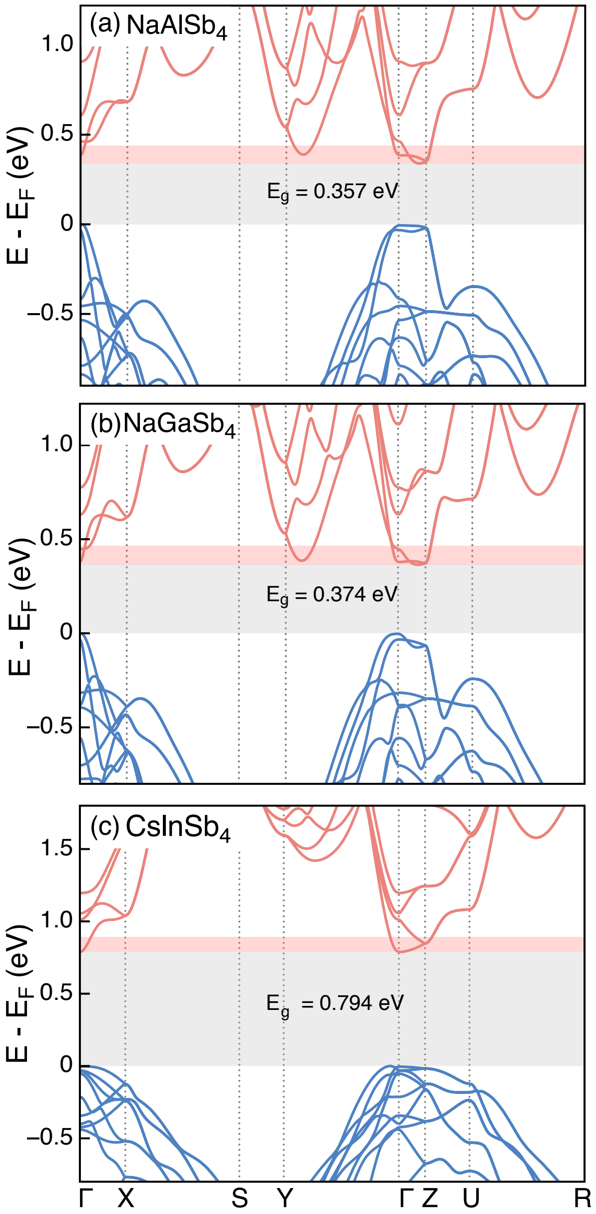

Fig. 6 Electronic band structures of (a) $NaAlSb_4$, (b) $NaGaSb_4$, and (c) $CsInSb_4$ along the special k-point paths of the Brillouin zone of an orthorhombic lattice. The grey shaded region shows the band gap and red shaded region indicates the 100 meV energy window used for fitting $m^*_{\mathrm{DOS,CB}}$ and extracting $N_{\mathrm{b,CB}}$. Note that the band edge positions are obtained from GW quasi-particle energy calculations.

3.4 Defect Chemistry of ABX_4 Zintl Phases

Although β serves to screen candidate TE materials, the successful prediction relies on a key assumption - the material must be optimally doped with electrons or holes, depending on n- or p-type TE. Materials with high β may be insulators or suffer from doping asymmetry. In such cases, the predicted TE performance cannot be realized. Therefore, we perform first-principles defect

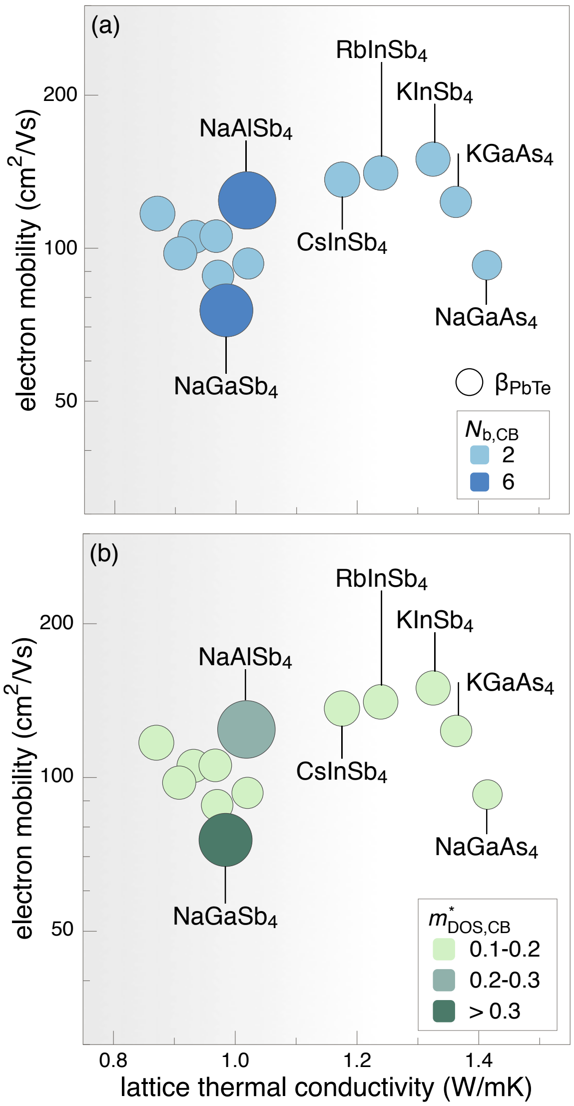

Fig. 7 Calculated n-type quality factor (β) plotted as a function of the computed room-temperature electron mobility and lattice thermal conductivity. The marker size scales with the value of β. For reference, the marker size corresponding to the β value of PbTe (15) is shown as a legend. The color scheme in (a) denotes the conduction band degeneracy ($N_{\mathrm{b,CB}}$) while in (b) the condunction band density-of-states (DOS) effective mass ($m^{*}_{\mathrm{DOS,CB}}$). The 7 newly predicted stable ABX$_4$ Zintl phases are labeled.

calculations to assess the dopability of the newly predicted candidate ABX$_4$ phases.

For defect calculations, we select the top three candidate materials (NaAlSb$_4$, NaGaSb$_4$, CsInSb$_4$) from Table 1 and assess their n-type dopability. These three candidate materials are composed of relatively earth-abundant and non-toxic elements. We assess the n-type dopability at the most alkali-rich condition within the phase stability region because the formation of the dominant electron-compensating, acceptor alkali vacancies is suppressed under those conditions. The acceptor cation vacancies, colloquially referred to as "killer defects", compensate electron doping by extrinsic dopants. The existence of cation vacancies with low formation energy is the primary cause of self p-type doping or difficulty in n-type doping in Zintl phases.[18] As such, Zintl phases where cation vacancies have high formation energies are considered n-type dopable. While n-type dopable Zintl phases are rare, we show here that our targeted search has enabled us to "design" as-yet-unknown Zintl phases with the desired doping characteristics as well as thermoelectric performance.

The calculated formation energies of native point defects (vacancies, anti-site defects and interstitials) in NaAlSb$_4$, NaGaSb$_4$ and CsInSb$_4$ under alkali-rich conditions are shown in Figure 8. The n-type dopability can be quantitatively assessed by ΔE_{don} - which is the energy "window" at CBM formed by the lowest-energy acceptor defects. If ΔE_{don} is large, then there is a better chance for n-type doping because of the limited electron compensation by the acceptor defects. The ΔE_{don} for NaAlSb$_4$, NaGaSb$_4$ and CsInSb$_4$ are large and positive - 0.34 eV, 0.30 eV and 0.47 eV under alkali-poor growth condition, respectively. In contrast, ΔE_{don} in well-known Zintl phases are typically negative. For example, ΔE_{don} for Ca$_5$Al$_2$Sb$_6$ is -0.1 eV.[18]

NaAlSb$_4$: The formation energies ($\Delta H_{\mathrm{D},q}$) of native point defects under Na-rich growth condition are shown in Figure 8(a). The lowest-energy acceptor defects are sodium vacancies V_{Na} and donors are anti-site defects $\mathrm{Sb}_{\mathrm{Al}}$ and Na interstitials Na_{i}. The equilibrium Fermi energy is usually in the vicinity of the intersection between the lowest-energy defects. In this case, the equilibrium Fermi energy lies around the mid-gap (marked by the dotted line in Figure 8). The predicted hole concentrations for undoped NaAlSb$_4$ is 6.5×10^{17} cm^{-3} at 800 K. However, what is more important is the high formation energy of acceptor Na vacancies, which creates a large n-type dopability window ΔE_{don} of 0.34 eV. Therefore, NaAlSb$_4$ is n-type dopable with high predicted n-type TE performance.

NaGaSb$_4$: The native defect energetics of NaGaSb$_4$ are similar to that of NaAlSb$_4$ (Figure 8b). The predominant native defects are $\mathrm{Sb}_{\mathrm{Ga}}$, Na_{i} and V_{Na}. The relatively high $\Delta H_{\mathrm{D},q}$ for V_{Na} creates a n-type dopability window of 0.30 eV. The smaller ΔE_{don} can be attributed to the slightly wider band gap of NaGaSb$_4$ (0.374 eV) compared to NaAlSb$_4$ (0.357 eV). The equilibrium Fermi energy in undoped NaGaSb$_4$ under Na-rich conditions is closer to the valence band maximum, with an estimated free hole concentration of 9.4×10^{17} cm^{-3} at 800 K synthesis temperature.

CsInSb$_4$: CsInSb$_4$ has a wider band gap (0.794 eV) than NaAlSb$_4$ and NaGaSb$_4$ due to the higher electronegativity difference between Cs and In. The native defect energetics of CsInSb$_4$ at Cs-rich growth condition are shown in Figure 8(c). The alkali vacancies V_{Cs} have even higher formation energy than V_{Na} in NaAlSb$_4$ and NaGaSb$_4$. Consequently, the n-type dopability window (ΔE_{don}) of 0.47 eV is quite large. Thus, CsInSb$_4$ is likely more n-type dopable than NaAlSb$_4$ or NaGaSb$_4$. In contrast with NaAlSb$_4$ and NaGaSb$_4$, p-type dopability of CsInSb$_4$ is limited by the low energy donor $\mathrm{Sb}_{\mathrm{In}}$ anti-site defects under Cs-rich growth conditions. Undoped CsInSb$_4$ is predicted to be lightly p-type with free hole concentration of 1.9×10^{17} cm^{-3}, assuming synthesis at 800 K.

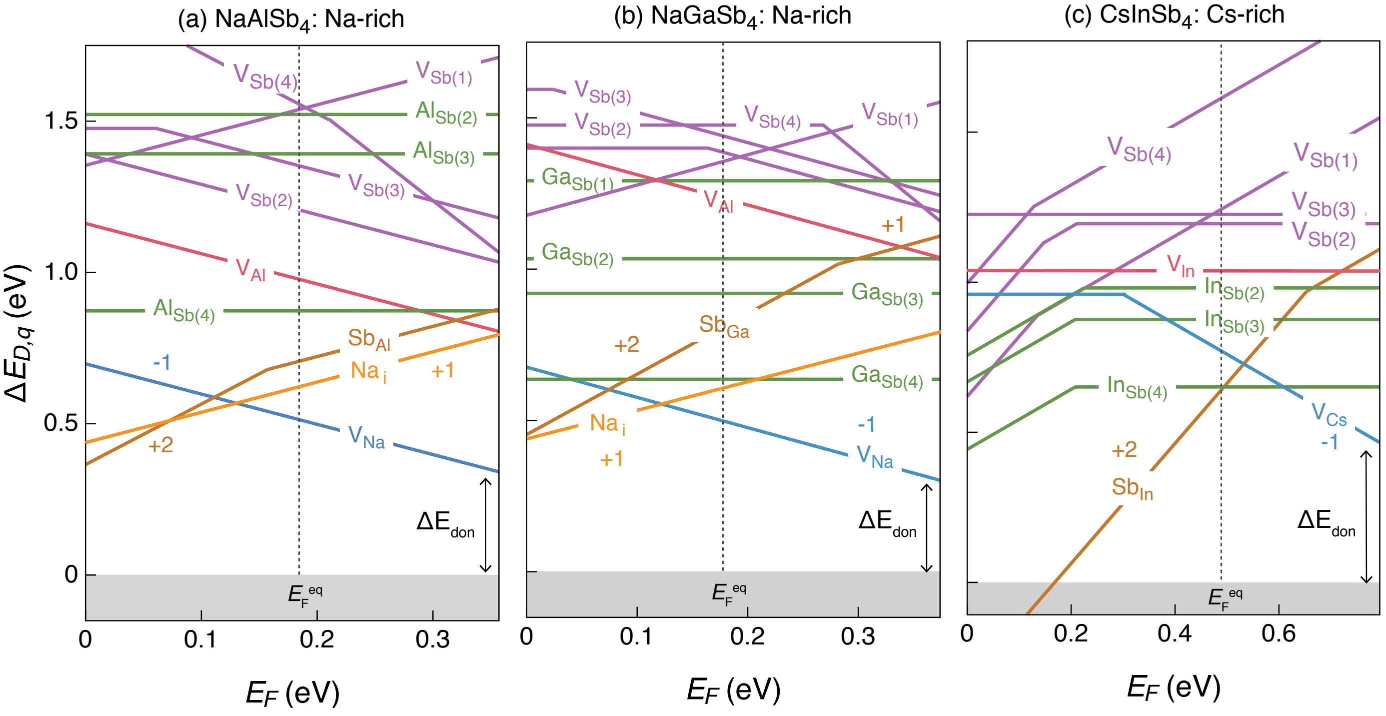

Fig. 8 Formation energies of native defects ($\Delta H_{D,q}$) as a function of Fermi energy (E_F) for (a) NaAlSb$_4$ (under Na-rich conditions), (b) NaGaSb$_4$ (under Na-rich condition), (c) CsInSb$_4$ (under Cs-rich condition). E_F is referenced to the valence band maximum and E_F values can range from 0 to the band gap. The line slope is equal to the charged state of the defect. The lowest energy acceptors are alkali vacancies (in blue), which restrict the ΔE_{don} to 0.34, 0.30 and 0.47 for NaAlSb$_4$, NaGaSb$_4$ and CsInSb$_4$ respectiviely. ΔE_{don} represents the n-type dopability window for extrinsic dopants. The equilibrium E_F is calculated at 800 K.

In summary, we find the three newly predicted ABX$_4$ Zintl phases, namely, NaAlSb$_4$, NaGaSb$_4$ and CsInSb$_4$, to be n-type dopable. Among these three candidates, CsInSb$_4$ has the largest n-type dopability window of 0.47 eV followed by NaAlSb$_4$ (0.34 eV) and NaGaSb$_4$ (0.30 eV). Furture work will explore possible extrinsic donor dopants to achieve optimal n-type doping that maximize the thermoelectric performance. In a prior study,[12] we found Ba to be an effective n-type dopant for KGaSb$_4$, with free electron concentrations exceeding 1×10^{19} cm^{-3}. This suggests that it may be possible to find suitable n-type dopants for the candidate phases, NaAlSb$_4$, NaGaSb$_4$ and CsInSb$_4$. The demonstration of n-type dopability of the new ABX$_4$ Zintl phases, constructed by chemical replacements, provides further confidence in the "doping by design" strategy undertaken in this study.

4 Conclusions

In this work, we utilize a new route to "design" materials with desired doping and functional characteristics. We hypothesize that the doping properties and functional performance of the prototype structure are translated to the new compounds created by chemical replacements, and we demonstrate this design strategy by discovering new n-type dopable ABX$_4$ Zintl phases. We perform first-principles calculations to explore 36 hypothetical ABX$_4$ Zintl phases in the KGaSb$_4$ structure, where A = Na, K, Cs, Rb, B = Al, Ga, In, and X = Sb, As, Bi, and assess their stability and n-type TE performance. We find 13 stable ABX$_4$ phases, including 6 known and 7 as-yet-unreported ABX$_4$ phases. Among the newly discovered phases, we consider the top candidates (NaAlSb$_4$, NaGaSb$_4$, CsInSb$_4$) with highest predicted n-type TE performance, and show that they are n-type dopable. The "doping by design" strategy demonstrated in this work offers an exciting route to discover new compounds with desired doping and functional performance and can be extended to discover new materials with applications beyond thermoelectrics.

Acknowledgements

JQ is funded by the NSF DIGI-MAT program, grant no. 1922758. PG and VS acknowledge support from NSF DMR program, grant no. 1729594. EE acknowledges support from NSF DMR program, grant no. 1729149. The research was performed using computational resources sponsored by the Department of Energy's Office of Energy Efficiency and Renewable Energy and located at the NREL.

References

1 J. He and T. M. Tritt, *Science*, 2017, **357**, 1.
2 P. Gorai, V. Stevanović and E. S. Toberer, *Nature Reviews Materials*, 2017, **2**, 1–16.
3 H. Mizoguchi, T. Kamiya, S. Matsuishi and H. Hosono, *Nature communications*, 2011, **2**, 1–5.
4 H. Kawazoe, M. Yasukawa, H. Hyodo, M. Kurita, H. Yanagi and H. Hosono, *Nature*, 1997, **389**, 939–942.
5 M. Chan, S. Lai, M. Fung, C. Lee and S. Lee, *Applied physics*

letters, 2007, **90**, 023504.

6 M. Y. Chan, S. L. Lai, M. K. Fung, C. S. Lee and S. T. Lee, *Applied Physics Letters*, 2007, **90**, 023504.

7 A. Janotti and C. G. Van de Walle, *Phys. Rev. B*, 2007, **76**, 165202.

8 P. Gorai, P. Parilla, E. S. Toberer and V. Stevanovic, *Chem. Mater.*, 2015, **27**, 6213.

9 L. Bjerg, G. K. H. Madsen and B. B. Iversen, *Chemistry of Materials*, 2012, **24**, 2111–2116.

10 P. J. Shaver and J. Blair, *Phys. Rev.*, 1966, **141**, 649–663.

11 B. R. Ortiz, P. Gorai, L. Krishna, R. Mow, A. Lopez, R. McKinney, V. Stevanović and E. S. Toberer, *Journal of Materials Chemistry A*, 2017, **5**, 4036–4046.

12 B. R. Ortiz, P. Gorai, V. Stevanovic and E. S. Toberer, *Chemistry of Materials*, 2017, **29**, 4523–4534.

13 B. R. Ortiz, P. Gorai, T. Braden, E. A. Bensen, S. D. Wilson, V. Stevanović and E. S. Toberer, *ACS Applied Energy Materials*, 2020, **3**, 2182–2191.

14 A. Balvanz, S. Baranets and S. Bobev, *J. Solid State Chem.*, 2020, **accepted**, 121476.

15 S. R. Brown, S. M. Kauzlarich, F. Gascoin and G. J. Snyder, *Chemistry of materials*, 2006, **18**, 1873–1877.

16 R. Marchand and W. Jeitschko, *Journal of Solid State Chemistry*, 1978, **24**, 351–357.

17 E. S. Toberer, A. Zevalkink, N. Crisosto and G. J. Snyder, *Advanced Functional Materials*, 2010, **20**, 4375–4380.

18 P. Gorai, A. Goyal, E. S. Toberer and V. Stevanović, *Journal of Materials Chemistry A*, 2019, **7**, 19385–19395.

19 P. Gorai, A. M. Ganose, A. Faghaninia, A. Jain and V. Stevanovic, *Materials Horizons*, 2020, DOI:10.1039/D0MH00197J.

20 R. Gautier, X. Zhang, L. Hu, L. Yu, Y. Lin, T. O. Sunde, D. Chon, K. R. Poeppelmeier and A. Zunger, *Nature chemistry*, 2015, **7**, 308.

21 X. Zhang, L. Yu, A. Zakutayev and A. Zunger, *Advanced Functional Materials*, 2012, **22**, 1425.

22 B. Meredig, A. Agrawal, S. Kirklin, J. E. Saal, J. W. Doak, A. Thompson, K. Zhang, A. Choudhary and C. Wolverton, *Phys. Rev. B*, 2014, **89**, 094104.

23 C. E. Wilmer, M. Leaf, C. Y. Lee, O. K. Farha, B. G. Hauser, J. T. Hupp and R. Q. Snurr, *Nature Chemistry*, 2012, **4**, 83.

24 Y. Hinuma, T. Hatakeyama, Y. Kumagai, L. A. Burton, H. Sato, Y. Muraba, S. Iimura, H. Hiramatsu, I. Tanaka, H. Hosono *et al.*, *Nature Comm.*, 2016, **7**, 1.

25 M. R. Filip and F. Giustino, *J. Phys. Chem. C*, 2016, **120**, 166.

26 A. Belsky, M. Hellenbrandt, V. L. Karen and P. Luksch, *Acta Crystallogr. B*, 2002, **58**, 364.

27 G. Kresse and J. Furthmüller, *Phys. Rev. B*, 1996, **54**, 11169–11186.

28 J. P. Perdew, K. Burke and M. Ernzerhof, *Phys. Rev. Lett.*, 1996, **77**, 3865–3868.

29 P. E. Blöchl, *Phys. Rev. B*, 1994, **50**, 17953–17979.

30 J. Yan, P. Gorai, B. Ortiz, S. Miller, S. A. Barnett, T. Mason, V. Stevanović and E. S. Toberer, *Energy Environ. Sci.*, 2015, **8**, 983–994.

31 S. A. Miller, P. Gorai, B. R. Ortiz, A. Goyal, D. Gao, S. A. Barnett, T. O. Mason, G. J. Snyder, Q. Lv, V. Stevanović and E. S. Toberer, *Chemistry of Materials*, 2017, **29**, 2494–2501.

32 F. Birch, *Journal of Geophysical Research*, 1952, **57**, 227–286.

33 V. Stevanović, S. Lany, X. Zhang and A. Zunger, *Phys. Rev. B*, 2012, **85**, 115104.

34 A. Togo, F. Oba and I. Tanaka, *Phys. Rev. B*, 2008, **78**, 134106.

35 A. Togo and I. Tanaka, *Scripta Materialia*, 2015, **108**, 1–5.

36 S. Lany and A. Zunger, *Phys. Rev. B*, 2008, **78**, 235104.

37 H. Peng, D. O. Scanlon, V. Stevanovic, J. Vidal, G. W. Watson and S. Lany, *Phys. Rev. B*, 2013, **88**, 115201.

38 A. Goyal, P. Gorai, H. Peng, S. Lany and V. Stevanovic, *Comp. Mater. Sci.*, 2017, **130**, 1.

39 W. Li, J. Carrete, G. K. H. Madsen and N. Mingo, *Phys. Rev. B*, 2016, **93**, 205203.

40 P. Gorai, D. Gao, B. Ortiz, S. Miller, S. A. Barnett, T. Mason, Q. Lv, V. Stevanovic and E. S. Toberer, *Computational Materials Science*, 2016, **112**, 368.

Electronic Supplementary Information:

Doping by Design: Finding New n-type ABX_4 Zintl Phases for Thermoelectrics

Jiaxing Qu,[†] Vladan Stevanović,[‡] Elif Ertekin,[†] and Prashun Gorai*,[‡]

[†] *University of Illinois at Urbana-Champaign, Urbana, IL 61801*

[‡] *Colorado School of Mines, Golden, CO 80401*

E-mail: pgorai@mines.edu

1. Fitted Elemental-Phase Reference Chemical Potentials

The fitted elemental-phase reference energies used in calculating the phase stability region (μ_i^0 in **Eq. 2**): Li: -1.74 eV, Na: -1.24 eV, K: -1.14 eV, Rb: -0.82 eV, Cs: -0.96 eV, Al: -3.55 eV, Ga: -3.12 eV, In: -2.62 eV, As: -4.59 eV, Sb: -4.11 eV, Bi: -4.19 eV

2. ABX$_4$ Structures from ICSD Considered for Assessing Structural Stability

$RbAlF_4$ (123), $KAlF_4$ (123), $CuGaCl_4$ (112), $CuGaI_4$ (82), $CuAuSe_4$ (11), $CuAlCl_4$ (112), $CuAlBr_4$ (112), $AgAuTe_4$ (13), $RbFeF_4$ (127), $NaMnF_4$ (14), $CsCrF_4$ (189), $RbFeF_4$ (18), $KAlF_4$ (11), $KFeF_4$ (63), $RbMnF_4$ (14), $RbFeF_4$ (57), $CsFeF_4$ (129), $TlAlF_4$ (15), $TlAlF_4$ (140), $LiMnO_4$ (63), $NaTiF_4$ (60), $KAuI_4$ (14), $KAuCl_4$ (14), $RbAlF_4$ (59), $LiAuF_4$ (13), $LiAuF_4$ (15), $CsAuF_4$ (71), $CsMnF_4$ (85), $AlInI_4$ (11), $TlMnF_4$ (15), $KTlF_4$ (144), $KScF_4$ (12), $KFeF_4$ (31), $CsReBr_4$ (61).

Numbers in parentheses denote the space group number.

3. Γ-point Frequencies of Phonon Modes

Table S1: Γ-point phonon frequencies of the 13 Zintl phases predicted to be stable in the $KGaSb_4$ structure type, given in THz. Only the 10 lowest frequency modes are shown, including the three acoustic modes.

	Phonon mode index									
Compound	1	2	3	4	5	6	7	8	9	10
$NaGaSb_4$	0.00	0.00	0.00	0.98	1.03	1.12	1.15	1.17	1.41	1.42
$NaAlSb_4$	0.00	0.00	0.00	0.61	0.66	0.68	0.79	0.80	0.93	0.93
$CsInSb_4$	-0.03	-0.02	0.00	0.54	0.57	0.58	0.59	0.65	0.70	0.87
$CsGaSb_4$	-0.01	0.00	0.00	0.60	0.70	0.72	0.76	0.78	0.79	0.97
$RbInSb_4$	0.00	0.00	0.00	0.55	0.57	0.59	0.64	0.68	0.69	0.90
$KInSb_4$	0.00	0.00	0.00	0.54	0.62	0.62	0.68	0.69	0.71	0.91
$CsAlSb_4$	-0.03	-0.01	0.01	0.61	0.65	0.67	0.73	0.79	0.79	0.94
$RbGaSb_4$	0.00	0.00	0.00	0.63	0.67	0.70	0.78	0.78	0.84	1.03
$KGaSb_4$	0.00	0.00	0.00	0.66	0.69	0.69	0.78	0.82	0.89	1.08
$RbAlSb_4$	0.00	0.00	0.00	0.65	0.67	0.68	0.77	0.78	0.84	1.04
$KGaAs_4$	0.00	0.00	0.00	0.98	1.03	1.07	1.09	1.24	1.30	1.58
$KAlSb_4$	0.00	0.00	0.00	0.64	0.71	0.71	0.78	0.81	0.89	1.09
$NaGaAs_4$	0.00	0.00	0.00	0.62	0.67	0.68	0.71	0.82	0.87	0.88

4. Electronic Structures of Stable ABX_4 Zintl Phases

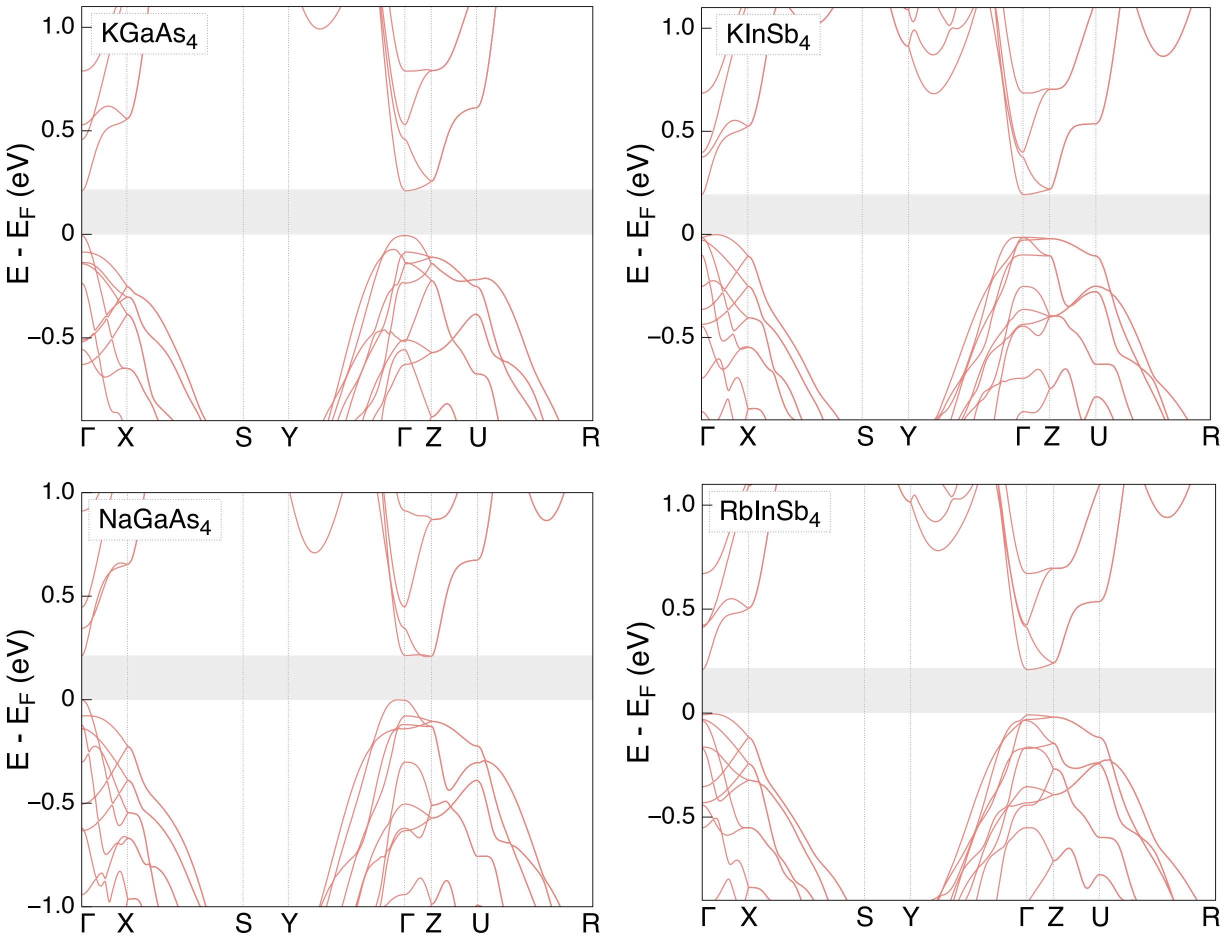

Figure S1: Electronic structures (GGA-PBE) of $KGaAs_4$, $KInSb_4$, $NaGaAs_4$, and $RbInSb_4$ along the special k-point paths of the Brillouin zone.

5. Predicted Thermoelectric Performance

Table S2: Computed electronic structure and transport parameters, and thermoelectric performance of 13 ABX_4 Zintl phases that are predicted to be stable in the $KGaSb_4$ structure. β is referenced to β of PbTe (15 for both *p*- and *n*-type). β_p and β_n are *p*- and *n*-type thermoelectric quality factor, E_g is DFT band gap, B is bulk modulus, $m^*_{\mathrm{DOS,VB}}$ and $m^*_{\mathrm{DOS,CB}}$ are density-of-states effective masses of valence and conduction bands, $N_{\mathrm{b,VB}}$ and $N_{\mathrm{b,CB}}$ are valence and conduction band degeneracies, μ_p and μ_n are room-temperature hole and electron mobilities, and κ_L is room-temperature lattice thermal conductivity.

Phases	$\beta_p/\beta_{\mathrm{PbTe}}$	$\beta_n/\beta_{\mathrm{PbTe}}$	E_g (eV)	B (GPa)	$m^*_{\mathrm{DOS,VB}}$ (m_e)	$m^*_{\mathrm{DOS,CB}}$ (m_e)	$N_{\mathrm{b,VB}}$	$N_{\mathrm{b,CB}}$	μ_p (cm^2/Vs)	μ_n (cm^2/Vs)	κ_{L} (W/mK)
$NaGaSb_4$	0.7	4.8	0.19	19.9	0.43	0.33	2	7	17	88	1.0
$NaAlSb_4$	0.7	4.5	0.12	19.8	0.43	0.24	2	6	17	124	1.0
$CsInSb_4$	1.0	1.7	0.25	29.0	1.59	0.14	4	2	7	136	1.2
$CsGaSb_4$	0.5	1.7	0.30	18.9	0.80	0.11	2	2	6	117	0.9
$RbInSb_4$	1.1	1.6	0.22	28.8	1.29	0.13	4	2	9	141	1.2
$KInSb_4$	1.5	1.6	0.19	30.3	1.32	0.13	5	2	12	150	1.3
$CsAlSb_4$	0.8	1.5	0.32	19.3	1.00	0.59	3	2	7	98	0.9
$RbGaSb_4$	1.1	1.5	0.30	19.0	0.51	0.12	3	2	19	105	0.9
$KGaSb_4$	0.3	1.5	0.25	19.2	0.30	0.12	1	2	14	106	1.0
$RbAlSb_4$	0.3	1.4	0.26	19.3	0.34	0.14	1	2	12	88	1.0
$KGaAs_4$	0.8	1.4	0.22	26.9	0.85	0.14	3	2	12	123	1.4
$KAlSb_4$	0.3	1.3	0.21	19.6	0.26	0.14	1	2	18	93	1.0
$NaGaAs_4$	0.5	1.2	0.21	28.2	0.71	0.18	2	2	11	93	1.4